COMMUNICATION

Functionalized Graphene Sheets as Molecular Templates for Controlled Nucleation and Self-Assembly of Metal Oxide-Graphene Nanocomposites

Xiaolin Li, Wen Qi, Donghai Mei, Maria L. Sushko, Ilhan Aksay, and Jun Liu*

Since its discovery,[1] graphene has been widely studied for electronics,[1–4] energy,[5–12] catalysis,[13–16] and sensing applications.[17,18] Functionalized graphene sheets (FGS) (or chemically derived graphene sheets),[19–21] along with other graphene materials including pristine graphene and graphene oxide (GO),[4,22] have been explored extensively because of their good electrical conductivity and tunable functional groups that are either retained after the chemical/physical reduction of graphene oxide or introduced during the exfoliation of graphite/expandable graphite.[19–25] Recently, FGS-metal oxide composites such as FGS-SnO_2, FGS-TiO_2, FGS-Co_3O_4, GO-mesoporous SiO_2, etc. have been prepared either by direct deposition or surfactant-mediated synthesis.[6,7,10–12,15,26]

Graphene not only serves as a key component of nanocomposite materials, it also is an ideal template to control the structures and properties of nanocomposite materials because of their good electronic and mechanical properties, two-dimensional nature of the structure and tunable surface chemistry. There are quite a few reports on the interaction between metal oxides and graphene.[27–30] Recently, it was reported that defects or functional groups on graphene could be the binding/reactive sites for Pt, sulfur, Li_2O_2, and indium tin oxide (ITO)/Pt in lithium batteries and fuel cell applications.[8,9,13,31] However, considering the wide interests in metal oxides (e.g., SnO_2, TiO_2, ZrO_2, etc.) and their composites for a broad range of applications,[6,7,10,11] a more systematic study on how the metal oxides interact with the graphene surface, and what kind of crystalline phases and new structures can be produced by controlling the surface chemistry, is desired.

In this paper, we combined theoretical and experimental study of the nucleation and self-assembly process in FGS-metal oxide systems (FGS-SnO_2, FGS-TiO_2, and FGS-ZrO_2). The aim of the paper is two-fold: i) to provide a general understanding of how graphene surface controls nucleation of metal oxides; and ii) to explore novel synthesis methods to control nucleation during self-assembly processes. For the first objective, we synthesized FGS-SnO_2 and FGS-TiO_2 and demonstrated that the functional groups on FGS surface determine the nucleation energy, and thus control the nucleation sites and nucleation density. We also demonstrated that FGS can tune the nucleation energies for different crystalline structures and thereby control the crystalline phases. For the second objective, we use FGS as a molecular template to direct the self-assembly of surfactant micellar structures and produce ordered, mesoporous arrays of crystalline metal oxide composites (FGS-mesoporous TiO_2 and FGS-mesoporous ZrO_2).

To reveal the role of functional groups on graphene sheets, templated nucleation and growth of metal oxides (e.g. SnO_2) is studied on FGS with different amounts of defects/functional groups. The relative content of functional groups associated with the defects is indicated by the C/O ratio.[4] A smaller C/O ratio reflects a higher number of functional groups on FGS. Therefore, the number of functional groups increases for FGS with a C/O ratio of 100 (FGS-100), to, 14 (FGS-14), to graphene oxides (GO, with a C/O ratio of ≈3).[4,22] As a result, the nucleation density of SnO_2 increases in the same order (**Figure 1**). The transmission electron microscopy (TEM) image in Figure 1a reveals a low SnO_2 density on FGS-100 with only parts of the surface covered. As the number of defect sites increase, more SnO_2 particles nucleate as shown for FGS-14 in Figure 1b. The GO-SnO_2 composite further corroborated this trend with the GO surface almost fully covered with a uniform layer of SnO_2 (Figure 1c). High-resolution TEM images (Figure 1d & 1e) also clearly showed a higher SnO_2 density on GO than on FGS-14.

Theoretical simulation confirms that the functional groups on FGS play a role of nucleation sites for metal oxides.[32–34] We show the result of the interaction between a carboxylic group on the graphene surface and the metal oxide to demonstrate that the nucleation energy of metal oxides can be changed significantly even with an individual functional group on the surface. Preliminary studies show that different oxygen-containing groups and different functionalization degree (or amounts of functional groups) have similar effects, although the exact nature of different functional groups and how it affects the nucleation need to be carefully studied in the future. Figure 1f shows the density functional theory (DFT) calculation of the nucleation energy for $(SnO_2)_n$ clusters on FGS with a carboxyl group linking to an embedded 5-8-5 defect (other functional groups like hydroxyl groups show similar trends, data not shown) and on pristine graphene (perfect graphene without defects/functional groups). The nucleation of SnO_2 on FGS is

Dr. X. L. Li, Dr. D. Mei, Dr. M. L. Sushko, Dr. J. Liu
Pacific Northwest National Laboratory
Richland, WA 99352, USA
E-mail: Jun.Liu@pnnl.gov
W. Qi
Department of Materials Science and Engineering
Tianjin University
Tianjin 300072, China
Dr. I. Aksay
Department of Chemical Engineering
Princeton University
Princeton, NJ 08544, USA

Materials
Views
www.MaterialsViews.com

ADVANCED
MATERIALS
www.advmat.de

COMMUNICATION
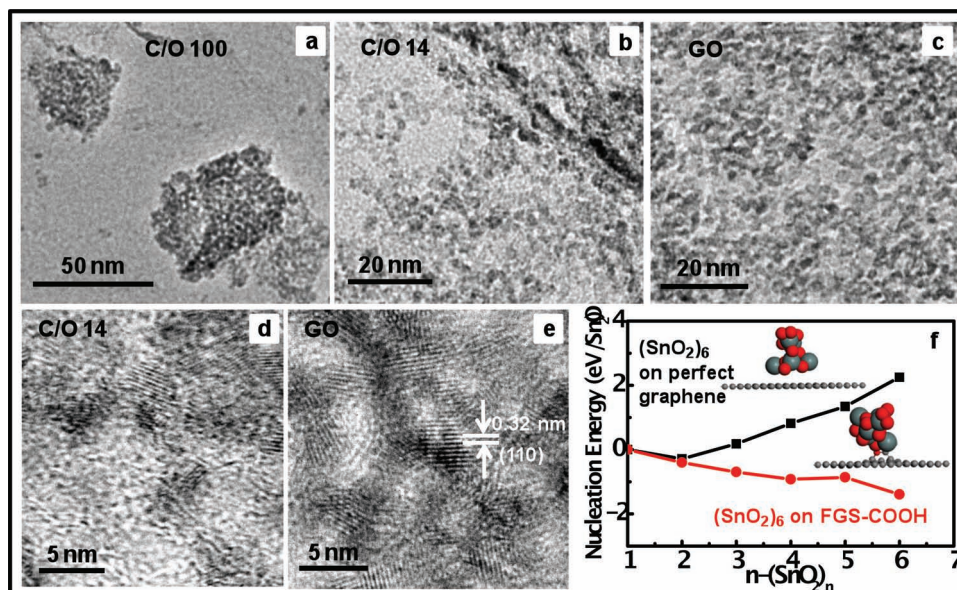
Figure 1. Experimental observation and theoretical simulation of the defect-directed nucleation of SnO_2 on FGS. a) SnO_2 nanoparticles on FGS (C/O = 100). b) SnO_2 nanoparticles on FGS (C/O = 14). c) SnO_2 nanoparticles on GO. d,e) High-resolution TEM images of SnO_2 nanoparticles on FGS (C/O = 14) and GO. f) DFT calculation of SnO_2 nucleation (free energy as a function of cluster size) on pristine graphene (black curve) and on FGS with a carboxylic group linking to the defect site (red curve).

energetically favorable with the nucleation energy decreasing by approximately –1.5 eV as the cluster size, n, increases from 1 to 6 (Figure 1f and Supporting information, Figure S1). On the other hand, on pristine graphene, there is a +2.0 eV energy penalty for $(SnO_2)_n$ clusters to grow from 1 to 6 (Figure 1f and Figure S2). The metal oxides prefer to nucleate and grow on the FGS surface because of the low nucleation energy at the functional groups sites. It explains why the nucleation density increases with the increase of the density of functional groups.

Other factors such as the edge and side of graphene also play important role for the nucleation of metal oxides, but our studies use FGS with a lateral dimension of several micrometers. What happens on the edge or the side of FGS is not studied.

The effect of FGS on nucleation is also observed on TiO_2 (**Figure 2**a,b). For both anatase and rutile phases, the nucleation processes on pristine graphene (Figure 2a & Figure S3) are energetically unfavorable (+0.47 eV energy increase for rutile-like TiO_2 and +2.79 eV energy increase for anatase-like TiO_2 as the cluster size increases from 3 to 24), but the formation of TiO_2 on FGS with a carboxyl group linking to an embedded 5-8-5 defect (Figures 2b & Figure S4) is thermodynamically favorable (–4 eV energy drop). As reference calculation, precipitation of bulk anatase and rutile TiO_2 is energetically favored in solution (Figure 2c).

In addition to controlling the nucleation sites, FGS can also alter the stability of a specific crystalline phase. TiO_2 obtained in solution without FGS has an anatase structure with small nanoparticles aggregated into secondary spherical particles of ≈50 to 200 nm in size (Figure 2d). Surprisingly, rutile-structured TiO_2 was formed with the addition of FGS under the same experimental conditions. Figure 2e shows that the composite with

rutile TiO_2 forms large, elongated, rod-shaped aggregates on FGS. The change of crystalline phase with and without FGS is also confirmed by X-ray diffraction patterns (Figure 2f).

DFT simulation corroborated the FGS-induced polymorph selection.[32–34] The interfacial interaction between FGS and metal oxide nanoparticles is believed to control the nucleation energy for different phases of TiO_2 leading to different crystallines. The change in nucleation energies for anatase- and rutile-phase TiO_2 without graphene support and on FGS is quite different. In bulk phase, anatase TiO_2 is more stable than rutile-structured TiO_2 by ≈ –0.43 eV without graphene support (Figure 2c & Figure S5). On FGS (e.g., a carboxyl group linking to an embedded 5-8-5 defect), the formation of rutile TiO_2 is energetically more favorable by ≈ –0.3 eV than forming anatase TiO_2 (Figure 2b & Figure S4), which is consistent with our experimental observations.

Results discussed above demonstrate that the nucleation on FGS and thereby the crystalline structure obtained, are determined by the functional groups on FGS surface, but the ability to increase the number of functional groups on native FGS is limited without significantly oxidizing the FGS. Another way to functionalize the graphene surface is to use bifunctional surfactants.[10,11,26] The use of surfactants can significantly lower the nucleation energy and facilitate the nucleation of metal oxides on FGS. **Figure 3**a shows the calculation of the nucleation of TiO_2 on FGS with a hydroxyl terminated ligand (–$CCH_2CH_2CH_2OH$) linking to the 5-8-5 defect. Most likely due to the flexibility and the spatial freedom provided by the ligand, the nucleation of anatase is favorable (Figure S6) and is similar to the solution precipitation without FGS (Figures 2c and Figure S5).

The above calculation shows that ligands and surfactants thus can be used to induce dense nucleation on FGS.[10,11] More
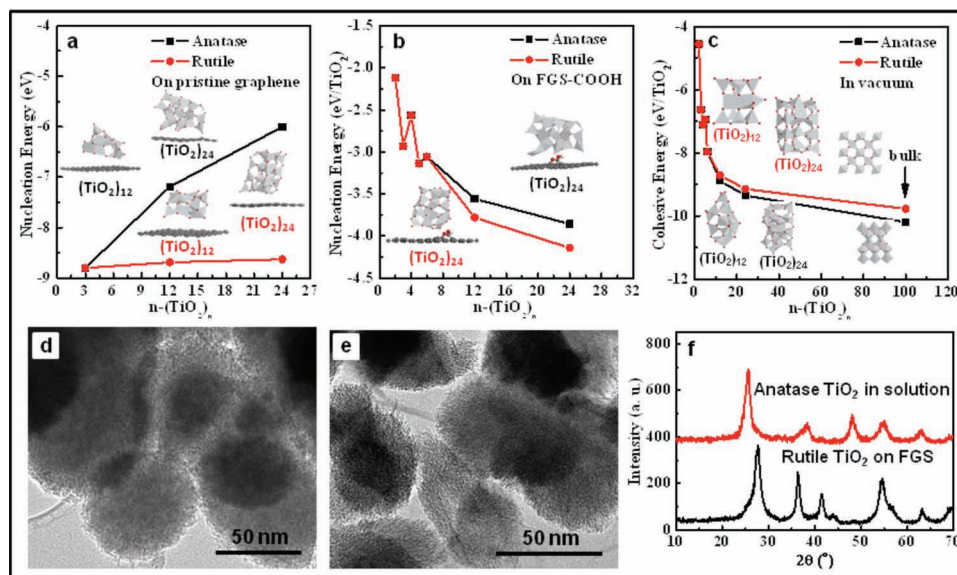
Figure 2. Experimental observation and theoretical simulation of the controlled nucleation and crystal growth of TiO_2 on pristine graphene, on FGS, and in vacuum. a) DFT calculation of TiO_2 nucleation on pristine graphene (free energy as a function of cluster size). b) DFT calculation of TiO_2 nucleation on FGS with a carboxylic group linking to the defect site. c) DFT calculation of the free energy of TiO_2 clusters as a function of sizes without graphene. d) TEM image of anatase TiO_2 produced in a solution. e) TEM image of rutile TiO_2 particles on FGS. f) XRD patterns of anatase TiO_2 produced in solution and rutile TiO_2 on FGS.

interestingly, previous studies showed that surfactants can form ordered hemi-micelle structures on graphite template and other surfaces along specific crystallographic directions[35–37] (Figure 3b). Graphite and other substrates thus have been used as templates for growing ordered mesophase silicate materials

via hydrothermal reactions.[38,39] However, there are two limitations for using these templates. Firstly, the hard substrate (graphite and silicon etc) template approach only produces supported films and structures, but not bulk, functional composite materials. Secondly, it is difficult to obtain ordered crystalline
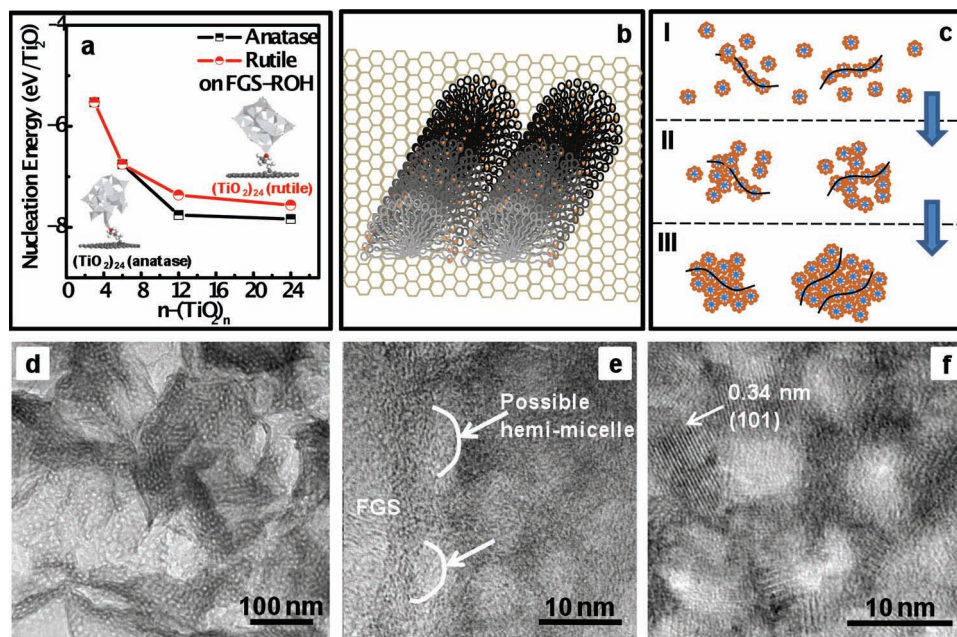
Figure 3. Synthesis of ordered crystalline mesoporous TiO_2 on FGS. a) DFT calculation of TiO_2 nucleation on FGS with an OH-terminated ligand. b) Graphene template with the formation of ordered surfactant micelle structures. c) Schematic illustration showing the structural evolution of the micelle-metal oxide-FGS composites upon drying. d) TEM image of ordered, amorphous mesoporous TiO_2 on FGS after self-assembly. e) TEM image showing possible hemi-micelles at the FGS interfaces. f) High-resolution TEM image of the crystalline mesoporous TiO_2 on FGS.

mesoporous metal oxides because the ordered surfactant structures are hard to maintain during crystal growth. Our study also suggested that only nanocrystalline films and layered structures can be obtained from the traditional hydrothermal reaction that is widely used in the literature.

In order to stablize the ordered micellar structure and control the crystal growth, we developed a graphene templated rapid evaporation and self-assembly method (GTES) to prepare ordered crystalline metal oxides on FGS. The GTES process, inspired by the rapid evaporation-induced self-assembly method,[40] is illustrated in Figure 3c. Firstly, FGS is dispersed in a pre-prepared solution of surfactants, acid, and metal oxide precursor. The surfactant molecules dispersed in the solution are likely to be absorbed on FGS surface as hemi-micelles (stage I).[35,36] During the drying process (stage II), the micelle and ceramic precursor concentration around FGS increase. The ceramic precursors gradually hydrolyze to form amorphous metal oxides. Upon further drying (stage III), the amorphous metal oxides and the surfactant micelles condense on FGS and self-assemble into ordered nanostructures. After the self-assembled structures are formed, the materials can be annealed to achieve desired nanocrystallites. Because of the physical confinement provided by the condensed, amorphous metal oxide matrix, the ordered structures are stable and resistant to deformation during crystallization.

The validity of this approach was confirmed experimentally. TEM and X-ray diffraction (XRD) characterizations show that after drying FGS-TiO$_2$ mesoporous composite is completely amorphous with pores of ≈6 to 10 nm (Figure 3d & Figure S7). Figure 3e shows a high-resolution TEM image of the interface between FGS and the mesophase TiO$_2$. Despite the poor contrast because of the amorphous nature of TiO$_2$, the possible hemi-micelle structures are visible close to FGS surface. It is difficult to image mesoporous metal oxide on single-layer FGS, therefore only few-layer FGS are shown here. The ordered mesostructures are maintained after annealing at 400 °C in argon. High-resolution TEM analysis reveals that the mesopores, ≈6–10 nm in diameter, are surrounded by ≈4 nm walls made of small TiO$_2$ crystals of ≈4 nm × 7 nm in size (Figure 3f & Figure S8). The selection area electron diffraction (image not shown) shows a typical anatase polycrystalline pattern. According to the results of thermal gravimetric analysis (TGA), more than 97 wt% of the surfactant is removed after annealing (Figure S9). Brunauer–Emmett-Teller (BET) and Barrett-Joyner-Halenda (BJH) measurements (Figure S10) show a surface area of ≈150 m^2/g and a pore size of ≈6.5 nm, which is consistent with the result of our TEM analysis.

To further demonstrate the surfactant effect on the synthesis of FGS-mesoporous TiO$_2$ nanocomposites, we performed control experiments and synthesized FGS-TiO$_2$ nanocomposites under the same conditions without using surfactants. As shown in Figure S11, TiO$_2$ nanoparticles are obtained on FGS surfaces instead of the ordered mesoporous structure.

It must be noted that since ordered micellar structures are only formed on crystalline hydrophobic/hydrophilic surfaces,[35,36] GO, which has extremely disordered graphitic plane,[4,22] leads to disordered micellar structures and the deposition of TiO$_2$ nanocrystallites instead of ordered mesoporous metal oxides (Figure S12). In contrast, FGS retains the ordered crystalline structure in its graphitic plane and hence supports the formation of ordered mesoporous materials. These results confirm the templating effect of the graphene surfaces for the ordered micellar structures.

The presented self-assembly approach is a general method and can be applicable to other metal oxides, such as, for example, FGS-mesoporous ZrO$_2$ composites. The composite obtained after drying is amorphous. Then, after annealing at 400 °C in argon, the surfactants were removed, and crystalline mesoporous composites formed, as indicated by the TEM analysis (**Figure 4**a & 4b), XRD (Figure S13), and TGA (Figure S14). The
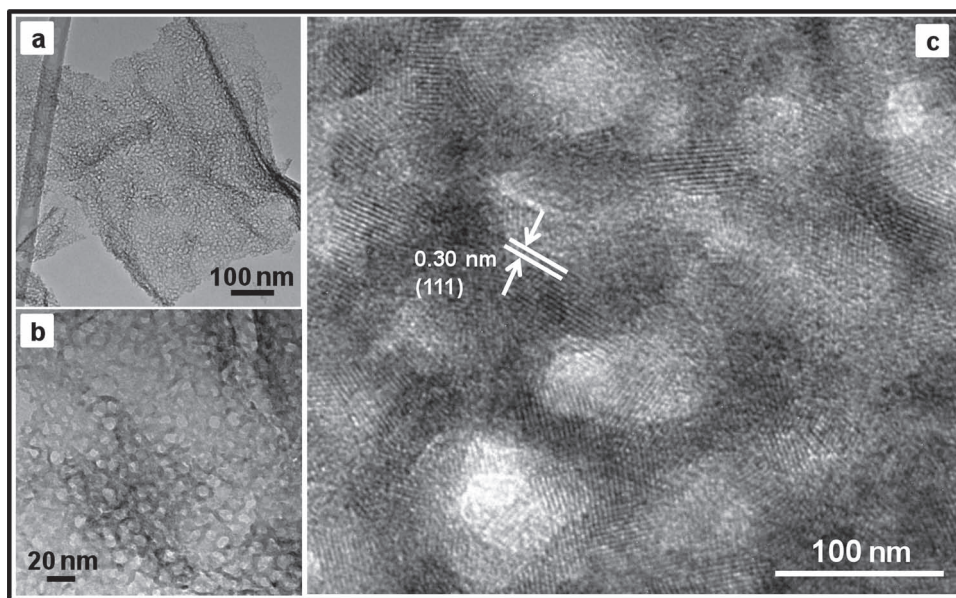
Figure 4. Ordered mesostructured ZrO$_2$ on FGS. a) FGS-mesoporous ZrO$_2$ composite after self-assembly. b) Crystalline mesoporous ZrO$_2$ on FGS after annealing at 400 °C in argon atmosphere. c) High-resolution TEM image of Figure 4b.

COMMUNICATION

crystalline structure can be either cubic or tetragonal phase, but the diffraction peaks are too broad to differentiate. The high-resolution TEM image (Figure 4c) reveals the crystalline nature of the walls, which are ≈4 nm thick with the pore dimension of ≈8 to 10 nm. We also have shown that ordered mesoporous mixed metal oxides, TiO_2 and ZrO_2, and a wide range of doped crystalline mesoporous metal oxides can be prepared in desired molar ratios. In the mixed phase, the crystallization temperature increases. For example, for a 50 wt% mixture of ZrO_2 and TiO_2, crystallization is not observed until 600 °C (Figure S15).

This paper emphasizes the understanding of the synthetic process of metal oxide-graphene nanocomposites. There is great opportunity to explore properties and potential applications of such materials, in particular the ordered, crystalline mesoporous metal oxide-graphene composites. We performed preliminary study on the Li-ion intercalation properties of mesoporous TiO_2-graphene composite as potential stable and fast charging anode materials for Li-ion batteries. Even without any optimization of the composition and experimental conditions, high rate capability and stability are observed (Figure S16 and supporting information).

In summary, we have demonstrated that FGS is a new class of molecular templates for controlling nucleation and self-assembly of graphene-metal oxide nanocomposites. The interfacial chemistry plays a key role in controlling the nucleation sites and crystalline phases. FGS can also direct the self-assembly of ordered micelle structures and ordered mesoporous nanocomposites, but the crystallization process must be controlled in order to maintain the ordered structure. Compared to other two-dimensional templating approaches, using FGS molecular templates provides a good opportunity to prepare novel bulk structured nanocomposite materials in which the template also serves as a key functional component to improve the properties such as electrical conductivity and mechanical stability. It is noteworthy that the novel synthesis method reported here was developed based on the fundamental understanding of the nucleation and assembly processes. The versatility of the graphene templated rapid evaporation and self-assembly approach paves the way for controlled scalable synthesis of new nanocomposite materials with well defined structure and properties for various applications.

Experimental Section

Functionalized Graphene Sheets and Graphene Oxide: The FGSs for this work were prepared by the thermal expansion of graphite oxide that contained ≈80% single-sheet graphene along with stacked graphene.[20,21] The carbon-to-oxygen ratios of the graphene materials were about 14 (FGS-14) and 100 (FGS-100), which allowed the FGSs to retain good electrical conductivity. Graphene oxide was synthesized by a modified Hummers method.[4,22] More-detailed information about the structures and properties of the FGS is included in the supporting information.

Synthesis of FGS-SnO$_2$ and FGS-TiO$_2$ Nanocomposites: For a typical preparation of the FGS-SnO$_2$ nanocomposites, FGS-14/FGS-100 (71.3 mg, Vobeck Materials) was added to water (≈40 mL) and sonicated for 10–15 min (Branson Sonifer S-450 A, 400 W). Then, a SnCl$_2$ solution (≈10 mL, 0.12 M in 3.8 wt% HCl) was added to the above dispersion while stirring. After that, a urea solution (≈4.8 mL, 1 M) and a H$_2$O$_2$ solution (≈4 mL, 1 wt%) were added dropwise under vigorous stirring. The resulting mixture was diluted to 100 mL and stirred at 90 °C for

16 h. The product was collected by centrifugation, washed with water, and dried in vacuum. For the synthesis of the GO-SnO$_2$, GO (≈71.3 mg) was used, replacing the FGS. The other conditions were the same as the synthesis of FGS-SnO$_2$.

The FGS-TiO$_2$ nanocomposite was synthesized using hydrothermal methods with titanium isopropoxide (Ti(Oipr)$_4$) as the precursor. FGS-14 (≈17 mg) was dispersed in H$_2$SO$_4$ (1 M, 40 mL) by 2 h sonication. After Ti(Oipr)$_4$ (≈0.71 g) was added to the suspension, the mixture then was transferred to a polytetrafluoroethylene (Teflon)-lined autoclave and heated to 100 °C. After cooling to room temperature, the product was collected by centrifugation, washed with water, and dried at 80 °C. A control experiment of TiO$_2$ synthesis was conducted at similar conditions without adding FGS.

The mesoporous metal oxides on FGS were synthesized using an evaporation-induced self-assembly approach. For FGS-mesoporous TiO$_2$, Ti(Oipr)$_4$ (≈1.082 g) was added into an ethanol solution (3 g) of P123 (≈0.2 g). Then, while stirring, concentrated HCl (0.592 mL) was added to the solution. FGS-14 (≈10 mg) was added to the solution while stirring, and the solution was filtered after 15 min. The product was heated to 400 °C in argon at a rate of 1 °C/min and then held at 400 °C for 4 h. For FGS-mesoporous ZrO$_2$, zirconium butoxide (≈0.6 g) was added to an ethanol solution (3 g) of P123 (≈0.2 g). Then concentrated HCl (0.247 mL) and acetic acid (0.29 mL) were added to the solution while stirring. FGS-14 (≈10 mg) was added to the solution and then filtered after 15 min. The product was heated to 400 °C in argon at a rate of 1 °C/min and held at 400 °C for 4 h.

Characterization: The TEM images were taken using a JEOL-2010 high-resolution transmission electron microscope. The XRD analysis was carried out on a Philips Xpert X-ray diffractometer using Cu K$_\alpha$ radiation (λ = 1.54 Å). The TGA and differential scanning calorimetry (DSC) were conducted using a TGA/DSC 1 (Mettler Toledo) thermogravimetric analyzer in argon at a scan rate of 5 °C/min from room temperature to 800 °C. The nitrogen sorption isotherms were obtained using a Quantachrome Autosorb automated gas sorption system at −196 °C. Specific surface areas and pore-size distributions were calculated using the BET theory and the BJH method based on the adsorption branches. The specific pore volumes were measured at a relative pressure of 0.99.

Computations: Periodic self-consistent DFT calculations were carried out using the Vienna ab initio simulation package (VASP) simulation code.[32] The projector-augmented-wave method, combined with a plane-wave cut-off energy of 400 eV was used to describe the core and valence electrons.[33] The Perdew-Burke-Ernzerhof form of the generalized gradient approximation[34] was implemented in all of the calculations. The Brillouin zone integration was performed using a (3 × 3 × 1) k-point mesh sampling scheme. The graphene substrate was modeled as a single sheet with a (6 × 6) supercell. A large vacuum layer of 20 Å was inserted between two sheets in the z direction. All of the atoms in the calculation system were allowed to relax during the geometry optimizations. Ground-state atomic geometries of the entire systems were obtained by minimizing the forces on each atom to below 0.05 eV/Å. The driving force for the nucleation of the metal oxide particles in vacuum, and on the clean or functionalized graphene substrates was described by the Gibbs free-energy change (i.e., $\Delta G = G_{(MO_2)_n} - G_{(MO_2)_{n-1}} - G_{MO_2}$) (M = Sn or Ti). In the case of TiO$_2$, the initial structures of rutile and anatase $(TiO_2)_{12}$ as well as $(TiO_2)_{24}$ particles were cut directly from the corresponding bulks. The additional computational details and results are given in the supporting information.

Supporting Information

Supporting Information is available from the Wiley Online Library or from the author.

Acknowledgements

[1] K. S. Novoselov, A. K. Geim, S. V. Morozov, D. Jiang, Y. Zhang, S. V. Dubonos, I. V. Grigorieva, A. A. Firsov, *Science* **2004**, *306*, 666.

[2] A. K. Geim, K. S. Novoselov, *Nat. Mater.* **2007**, *6*, 183.

[3] X. L. Li, X. R. Wang, L. Zhang, S. W. Lee, H. J. Dai, *Science* **2008**, *319*, 1229.

[4] X. L. Li, G. Y. Zhang, X. D. Bai, X. M. Sun, X. R. Wang, E. G. Wang, H. J. Dai, *Nat. Nanotechnol.* **2008**, *3*, 538.

[5] S. Watcharotone, D. A. Dikin, S. Stankovich, R. Piner, I. Jung, G. H. B. Dommett, G. Evmenenko, S. E. Wu, S. F. Chen, C. P. Liu, S. T. Nguyen, R. S. Ruoff, *Nano Lett.* **2007**, *7*, 1888.

[6] S. M. Paek, E. J. Yoo, I. Honma, *Nano Lett.* **2009**, *9*, 72.

[7] N. Li, G. Liu, C. Zhen, F. Li, L. L. Zhang, H.-M. Cheng, *Adv. Funct. Mater.* **2011**, *21*, 1717.

[8] L. W. Ji, M. M. Rao, H. M. Zheng, L. Zhang, Y. C. Li, W. H. Duan, J. H. Guo, E. J. Cairns, Y. G. Zhang, *J. Am. Chem. Soc.* **2011**, *133*, 18522.

[9] J. Xiao, D. H. Mei, X. L. Li, W. Xu, D. Y. Wang, G. Graff, W. Bennett, Z. M. Nie, L. Saraf, I. Aksay, J. Liu, J.-G. Zhang, *Nano Lett.* **2011**, *11*, 5071.

[10] D. H. Wang, D. W. Choi, J. Li, Z. G. Yang, Z. M. Nie, R. Kou, D. H. Hu, C. M. Wang, L. V. Saraf, J. G. Zhang, I. A. Aksay, J. Liu, *ACS Nano* **2009**, *3*, 907.

[11] D. H. Wang, R. Kou, D. W. Choi, Z. G. Yang, Z. M. Nie, J. Li, L. V. Saraf, J. G. Zhang, G. L. Graff, J. Liu, M. A. Pope, I. A. Aksay, *ACS Nano* **2010**, *4*, 1587.

[12] H. L. Wang, L. F. Cui, Y. Yang, H. S. Casalongue, J. T. Robinson, Y. Y. Liang, Y. Cui, H. J. Dai, *J. Am. Chem. Soc.* **2010**, *132*, 13978.

[13] R. Kou, Y. Y. Shao, D. H. Mei, Z. M. Nie, D. H. Wang, C. M. Wang, V. V. Viswanathan, S. Park, I. A. Aksay, Y. H. Lin, Y. Wang, J. Liu, *J. Am. Chem. Soc.* **2011**, *133*, 2541.

[14] Y. G. Li, H. L. Wang, L. M. Xie, Y. Y. Liang, G. S. Hong, H. J. Dai, *J. Am. Chem. Soc.* **2011**, *133*, 7296.

[15] Y. Y. Liang, Y. G. Li, H. L. Wang, J. G. Zhou, J. Wang, T. Regier, H. J. Dai, *Nat. Mater.* **2011**, *10*, 780.

[16] G. M. Scheuermann, L. G. Rumi, P. Steurer, W. Bannwarth, R. Mulhaupt, *J. Am. Chem. Soc.* **2009**, *131*, 8262.

[17] F. Schedin, A. K. Geim, S. V. Morozov, E. W. Hill, P. Blake, M. I. Katsnelson, K. S. Novoselov, *Nat. Mater.* **2007**, *6*, 652.

[18] Y. Wang, Z. H. Li, D. H. Hu, C. T. Lin, J. H. Li, Y. H. Lin, *J. Am. Chem. Soc.* **2010**, *132*, 9274.

[19] S. J. Park, R. S. Ruoff, *Nat. Nanotechnol.* **2009**, *4*, 217.

[20] H. C. Schniepp, J.-L. Li, M. J. McAllister, H. Sai, M. Herrera-Alonso, D. H. Adamson, R. K. Prud'homme, R. Car, D. A. Saville, I. A. Aksay, *J. Phys. Chem. B* **2006**, *110*, 8535.

[21] M. J. McAllister, J.-L. Li, D. H. Adamson, H. C. Schniepp, A. A. Abdala, J. Liu, M. Herrera-Alonso, D. L. Milius, R. Car, R. K. Prud'homme, I. A. Aksay, *Chem. Mater.* **2007**, *19*, 4396.

[22] W. S. Hummers, R. E. Offeman, *J. Am. Chem. Soc.* **1958**, *80*, 1339.

[23] K. N. Kudin, B. Ozbas, H. C. Schniepp, R. K. Prud'homme, I. A. Aksay, R. Car, *Nano Lett.* **2008**, *8*, 36.

[24] H. C. Schniepp, K. N. Kudin, J.-L. Li, R. K. Prud'homme, R. Car, D. A. Saville, I. A. Aksay, *ACS Nano* **2008**, *2*, 2577.

[25] J. L. Sabourin, D. M. Dabbs, R. A. Yetter, R. L. Dryer, I. A. Aksay, *ACS Nano* **2009**, *3*, 3945.

[26] Z.-M. Wang, W. D. Wang, N. Coombs, N. Soheilnia, G. A. Ozin, *ACS Nano.* **2010**, *4*, 7437.

[27] J. Hassoun, G. Derrien, S. Panero, B. Scrosati, *Adv. Mater.* **2008**, *20*, 3169.

[28] J. S. Zhou, H. H. Song, L. L. Ma, X. H. Chen, *RSC Adv.* **2011**, *1*, 782.

[29] D. Eder, *Chem. Rev.* **2010**, *110*, 1348.

[30] G. S. Hong, S. M. Tabakman, K. Welsher, H. L. Wang, X. R. Wang, H. J. Dai, *J. Am. Chem. Soc.* **2010**, *132*, 15920.

[31] D.-H. Lim, J. Wilcox, *J. Phys. Chem. C* **2011**, *115*, 22742.

[32] G. Kresse, J. Furthmuller, *Phys. Rev. B: Condens. Matter* **1996**, *54*, 11169.

[33] J. P. Perdew, K. Burke, M. Ernzerhof, *Phys. Rev. Lett.* **1996**, *77*, 3865.

[34] G. Kresse, D. Joubert, *Phys. Rev. B: Condens. Matter* **1999**, *59*, 1758.

[35] S. Manne, H. E. Gaub, *Science* **1995**, *270*, 1480.

[36] S. O. Nielsen, G. Srinivas, C. F. Lopez, M. L. Klein, *Phys. Rev. Lett.* **2005**, *94*, 228301.

[37] M. L. Sushko, J. Liu, *J. Phys. Chem. B* **2010**, *114*, 3847.

[38] P. D. Yang, D. Y. Zhao, D. I. Margolese, B. F. Chmelka, G. D. Stucky, *Nature* **1998**, *396*, 152.

[39] I. A. Aksay, M. Trau, S. Manne, I. Honma, N. Yao, L. Zhou, P. Fenter, P. M. Eisenberger, S. M. Gruner, *Science* **1996**, *273*, 892.

[40] A. Sellinger, P. M. Weiss, A. Nguyen, Y. F. Lu, R. A. Assink, W. L. Gong, C. J. Brinker, *Nature* **1998**, *394*, 256.